electronic reprint

Acta Crystallographica Section D
Biological Crystallography
ISSN 0907-4449

The high-mosaicity illusion: revealing the true physical characteristics of macromolecular crystals

Henry D. Bellamy, Edward H. Snell, Jeff Lovelace, Matthew Pokross and Gloria E. O. Borgstahl

Acta Crystallographica Section D
Biological Crystallography
ISSN 0907-4449

The high-mosaicity illusion: revealing the true physical characteristics of macromolecular crystals

Henry D. Bellamy,[a] Edward H. Snell,[b] Jeff Lovelace,[c] Matthew Pokross[c] and Gloria E. O. Borgstahl[c]*

[a]Stanford Synchrotron Radiation Laboratory, PO Box 4349, MS 69, Stanford, California 94309, USA, [b]NASA Laboratory for Structural Biology, Code SD48, Marshall Space Flight Center, Huntsville, AL 35812, USA, and [c]The University of Toledo, Department of Chemistry, 2801 West Bancroft Street, Toledo, OH 43606, USA

Correspondence e-mail: gborgst@uoft02.utoledo.edu

Received 28 January 2000
Accepted 16 May 2000

PDB Reference: MnSOD, 1d5n.

Typical measurements of macromolecular crystal mosaicity are dominated by the characteristics of the X-ray beam and as a result the mosaicity value given during data processing can be an artifact of the instrumentation rather than the sample. For physical characterization of crystals, an experimental system and software have been developed to simultaneously measure the diffraction resolution and mosaic spread of macromolecular crystals. The contributions of the X-ray beam to the reflection angular widths were minimized by using a highly parallel, highly monochromatic synchrotron source. Hundreds of reflection profiles over a wide resolution range were rapidly measured using a charge-coupled device (CCD) area detector in combination with superfine φ-slicing data collection. The Lorentz effect and beam contributions were evaluated and deconvoluted from the recorded data. Data collection and processing is described. From 1° of superfine φ-slice data collected on a crystal of manganese superoxide dismutase, the mosaicities of 260 reflections were measured. The average mosaicity was 0.0101° (s.d. 0.0035°) measured as the full-width at half-maximum (FWHM) and ranged from 0.0011 to 0.0188°. Each reflection profile was individually fitted with two Gaussian profiles, with the first Gaussian contributing 55% (s.d. 9%) and the second contributing 35% (s.d. 9%) of the reflection. On average, the deconvoluted width of the first Gaussian was 0.0054° (s.d. 0.0015°) and the second was 0.0061° (s.d. 0.0023°). The mosaicity of the crystal was anisotropic, with FWHM values of 0.0068, 0.0140 and 0.0046° along the *a*, *b* and *c* axes, respectively. The anisotropic mosaicity analysis indicates that the crystal is most perfect in the direction that corresponds to the favored growth direction of the crystal.

1. Introduction

The use of reflection mosaicity as an indicator of macromolecular crystal perfection was pioneered by Shaikevitch & Kam (1981). Subsequently, Helliwell and coworkers made use of synchrotron radiation to minimize the geometric and spectral contributions of the X-ray source to the experimental data (Colapietro *et al.*, 1992; Helliwell, 1988). Mosaicity analysis of chicken egg-white lysozyme, apocrustacyanin C and thaumatin crystals established a physical basis for the improvements seen in some microgravity-grown samples. In these samples, a reduction in the mosaic spread produced a corresponding increase in the signal-to-noise ratio of the reflection (Ng *et al.*, 1997; Snell *et al.*, 1995, 1997). The minimum mosaicities recorded were 0.005° for lysozyme, 0.030° for apocrustacyanin C_1 and 0.018° for thaumatin

measured at the full-width at half-maximum (FWHM). These values were obtained by deconvoluting the spectral and geometric contributions of the X-ray beam from the recorded rocking width, which allowed a quantitative comparison between samples (Colapietro *et al.*, 1992). Without such deconvolution, it is impossible to make quantitative comparisons between different experiments.

Successful measurement of mosaicity requires that the geometric and spectral parameters of the instrumentation do not mask the crystal characteristics. Synchrotron radiation is an ideal tool for these studies, as it can provide a highly parallel and (when a suitable monochromator is used) a highly monochromatic beam (Helliwell, 1992; Margaritondo, 1995). In previous studies, reflections were recorded individually with a scintillation counter mounted in the equatorial (vertical) plane by rotating the crystal about the horizontal axis (Colapietro *et al.*, 1992; Fourme *et al.*, 1995; Helliwell, 1988; Ng *et al.*, 1997; Snell *et al.*, 1995). This experimental setup minimized the Lorentz effect and eliminated the contribution from the horizontal beam divergence of the synchrotron beam. Ferrer & Roth (1998) developed an algorithm and software for mosaic spread analysis using data from an area detector. Here, this approach has been adapted and improved by using superfine φ-slicing data collection, unfocused monochromatic synchrotron radiation and a charge-coupled device (CCD) X-ray area detector.

Technology routinely employed in protein structure determination was adapted for mosaic spread analysis. A CCD area detector was used to rapidly record many reflections simultaneously and standard protein crystallography software was used to assign indices to each reflection and to obtain standard crystallographic statistics such as $I/\sigma(I)$ and resolution. Because the data are not all on the equatorial plane, horizontal divergence now becomes a contributor to the recorded rocking width in addition to the vertical divergence and spectral spread contributions present in other methods. These effects must be deconvoluted from the data so that the true crystal mosaicity can be evaluated and the advantages of an area detector realised. The CCD area detector allows a short exposure time and fast readout, so the superfine φ-slicing technique becomes practical. In this paper, the development of the crystal-quality evaluation technique and the deconvolution of the beam divergence, spectral divergence and Lorentz effects from the measured rocking widths of the reflections is described. The data processing is described, along with an example of the technique using a single crystal of manganese superoxide dismutase (MnSOD).

2. Theory

The mosaic nature of crystals was proposed by Darwin (1922) and approximates the crystal to a series of perfectly ordered volumes (domains) slightly misaligned with respect to each other. The reflection profile is broadened by the misalignment between domains, the volume of the domains (from Fourier truncation) and any lattice variation between them (Boggon *et al.*, 2000; Nave, 1998). Therefore, mosaicity is a measure of the long-range order within the crystal.

The width of the reflection profile is also broadened by the geometric and spectral parameters of the X-ray source used (Greenhough & Helliwell, 1982). The vertical and horizontal crossfire angles at the sample, γ_v and γ_h, respectively, together with the wavelength dispersion $\delta\lambda/\lambda$ contribute to the reflection broadening. Additionally, differences in the motion of reciprocal-lattice points through the Ewald sphere broaden reflections by varying amounts. The Lorentz correction (L) compensates for this effect. The angular width, φ_R, for a reflection in the case of a horizontal rotation axis and a Gaussian profile is given by (1), adapted from Helliwell (1992),

$$|\varphi_R| = (L^2\zeta^2\gamma_h^2 + \gamma_v^2)^{1/2} + \frac{L}{d}\cos\theta_{hkl}\left[\eta + \left(\frac{\delta\lambda}{\lambda}\right)\tan\theta_{hkl}\right]. \quad (1)$$

Here, η is the mosaic spread, ζ is the position of the corresponding reciprocal-lattice point projected onto the rotation axis and d is the resolution ($d = \lambda/2\sin\theta_{hkl}$). In (1), the correlated dispersion is ignored. In §3.2, this assumption is justified for the experimental setup used. If h and v are the horizontal (along the rotation axis) and vertical distance of the observed reflection from the direct-beam position, respectively, then ζ is given by

$$\zeta^2 = \left(\frac{h^2}{h^2 - v^2}\right)\sin^2(2\theta_{hkl}). \quad (2)$$

The Lorentz correction is given by

$$L = \frac{1}{[\sin^2(2\theta_{hkl}) - \zeta^2]^{1/2}}. \quad (3)$$

The reflection angle $2\theta_{hkl}$ is given by

$$2\theta_{hkl} = \tan^{-1}\left[\frac{(h^2 + v^2)^{1/2}}{\mathrm{XTD}}\right], \quad (4)$$

where XTD is the crystal-to-detector distance.

It can be seen in (1) that γ_v broadens the reflections universally over the detector, whereas γ_h broadens the reflection profile by an amount that depends on the position of the reflection. The Lorentz effect is maximal along the rotation axis, which is horizontal in the present case. The

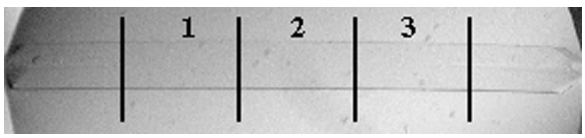

Figure 1
A long single crystal of *E. coli* MnSOD grown from 50 m*M* Bicine pH 8.5 and 25% PEG 6000. This crystal was square in cross section (120 × 120 µm), over 1 mm long and was cut into several pieces each approximately 250 µm long along the lines indicated. Pieces 2 and 3 were cryocooled and diffraction data were collected at SSRL beamline 7-1 for structure determination. The structure was determined using data from piece 3. Piece 1 was mounted in a capillary and room-temperature crystal mosaicity measurements were taken at SSRL beamline 1-5 in unfocussed mode using superfine φ-slicing the following day.

wavelength-dispersion term has its largest effect on high-resolution reflections. To evaluate the mosaicity of the crystal sample accurately, the crossfire angles and wavelength-dispersion terms need to be as small as possible. A properly configured synchrotron beamline can deliver a very parallel intense X-ray beam with little wavelength dispersion. Mosaicity is calculated from the measured reflection widths by rearranging (1),

$$\eta = \frac{|\varphi_R| - (L^2\zeta^2\gamma_h^2 + \gamma_v^2)^{1/2}}{(L/d)\cos\theta_{hkl}} - \left(\frac{\delta\lambda}{\lambda}\right)\tan\theta_{hkl}. \qquad (5)$$

3. Experimental

3.1. Crystal sample

MnSOD from *Escherichia coli* was purified and crystallized as described in Borgstahl *et al.* (2000). The space group was $C222_1$, with unit-cell parameters $a = 99.1$, $b = 107.3$, $c = 179.1$ Å. The asymmetric unit was composed of two MnSOD homodimers. A long single crystal was cut into several pieces (Fig. 1). High-resolution cryocooled diffraction data were collected from one of the pieces at Stanford Synchrotron Radiation Laboratory (SSRL) beamline 7-1. The crystal diffracted to 1.3 Å resolution, but in order to obtain adequate reflection separation it was necessary to collect data at a distance that only allowed 1.55 Å data to be recorded. Data were 100% complete with $R_{\rm sym}(I) = 7.0\%$ overall and $R_{\rm sym}(I) = 24.1\%$ in the highest resolution shell (1.55–1.64 Å). Data redundancy was 1.7-fold overall. Refinement and structural results have been reported elsewhere (Borgstahl *et al.*, 2000). Data reduction with *MOSFLM* (Leslie, 1990, 1999; Steller *et al.*, 1997; Powell, 1999) measured the crystal mosaicity to be 0.7°. It should be noted that this average mosaicity includes contributions from the focused synchrotron beam (∼0.3°) plus the true crystal mosaicity (increased by cryocooling).

3.2. Fine-slicing data collection

For mosaicity analysis, another piece of the MnSOD crystal was mounted in a sealed 0.7 mm glass capillary with the long axis of the crystal along the capillary axis. Slugs of mother liquor were placed at both ends of the capillary. No visible crystal defects were noted.

Data were collected at SSRL beamline 1-5 operating in unfocused mode. The FWHM of the vertical and horizontal divergences of the beam were calculated to be 19.5 and 48 µrad, respectively. The wavelength was calibrated by measuring the X-ray absorption edge of a metal foil. All data were collected at a wavelength of 1.000 Å. The wavelength dispersion from the double-crystal Si(111) monochromator was calculated to be 2.43×10^{-4}. The correlated dispersion of the beam at the sample position was calculated to be 2.50×10^{-4} Å mm^{-1} in the vertical direction. There is no horizontal dispersion. Since the sample crystal as mounted was only 0.2 mm in the vertical direction, the difference in average wavelength over the extent of the crystal was 5.0×10^{-5} Å. This value is small enough relative to the wavelength dispersion from the monochromator to justify dropping the term for correlated dispersion from (1), particularly for the relatively low resolution limit of the data in this study. An ADSC Quantum 4 CCD detector was used to collect the data. The detector was operated in 2×2 binned mode for faster readout. To save time during data collection, dezingering (*i.e.* taking two identical exposures and removing differences to compensate for the detection of random environmental radiation) was not used.

Crystal temperature was maintained at 295 ± 0.1 K using an FTS air-stream system. The crystal-to-detector distance was 260 mm. For crystal orientation, unit-cell parameter determination, indexing and assessment of diffraction resolution, 1° oscillations of 60 s duration were collected over two 2.0° φ ranges separated by 45° (Fig. 2). For mosaicity analysis, still images separated by 0.001° of 5 s duration were then collected over a 1° φ range (83 min °$^{-1}$). The optimum range for superfine data collection was selected by examining the 1.0° images. Reduction gearing enabled the φ axis to move in steps as small as 0.0005°.

3.3. Data processing

The MnSOD diffraction data were processed in three steps (Fig. 2). In the first step, the 1° oscillation images are autoindexed and integrated using *MOSFLM* and then scaled together with *SCALA* using smooth scaling (Collaborative Computational Project, Number 4, 1994; Evans, 1997; Kabsch, 1988; Leslie, 1999; Powell, 1999). This step provides traditional statistics on crystal quality, including the agreement between symmetry-related reflections $R_{\rm sym}$ and the signal-to-noise ratio $I/\sigma(I)$. The orientation matrix is then used in the second step to integrate the 1° oscillation image that corresponds with the

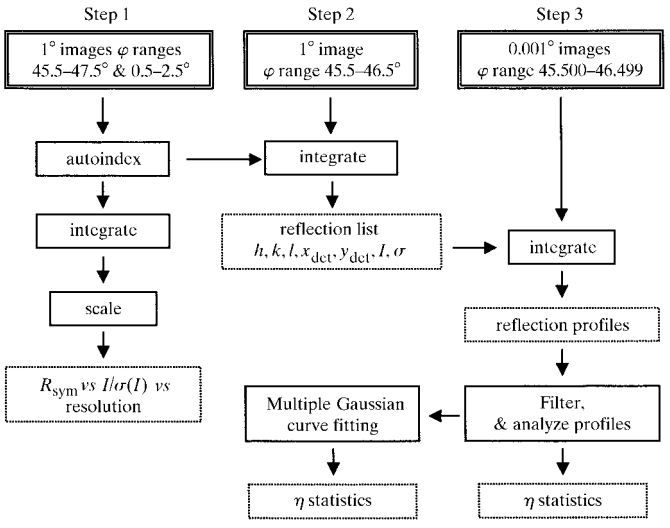

Figure 2
Flow diagram of the three steps involved in processing the MnSOD diffraction data. *MOSFLM* was used in steps 1 and 2 for autoindexing and integration. Integration in step 3 was performed with software provided by ADSC Inc. Software written by the authors was used for all other parts of step 3. The overall data processing was managed by a graphical user interface called *BEAM-ish* (Lovelace *et al.*, 2000).

superfine φ-sliced images. *MOSFLM* outputs a reflection list (called the mtz file) that includes the indices for each reflection along with its detector coordinates and estimated error. By default, *MOSFLM* omits reflections from this reflection list with widths greater than 5° owing to the Lorentz effect. Such reflections were therefore not used in the following mosaicity analysis.

In the third step, the mosaicity data from the crystal was obtained by integrating the superfine φ-sliced data with software provided by ADSC. All the 0.001° images were integrated at the *MOSFLM*-predicted reflection coordinate positions for reflections with $I/\sigma(I) > 3.5$; the output contained integrated intensities for each reflection for each image. Random radiation events in the phosphor or optical taper (known as 'zingers') were then removed from the diffraction data, reflection profiles were located and the reflection width and the true crystal mosaicity η were calculated. Zingers were identified as extremely large intensities that existed on only one image. The zingers were erased and replaced with the average intensity of the neighboring images. To remove noise from the data, a three-point moving average filter was applied.

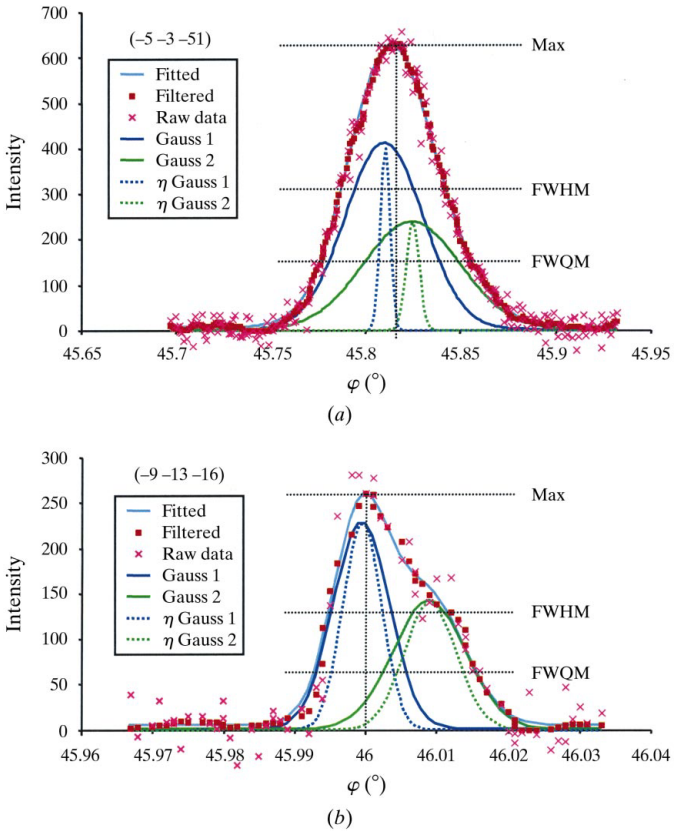

Figure 3
Examples of reflection profiles and Gaussian fits: (*a*) The (−5 −3 −51) reflection was broadened by Lorentz and beam effects and the measured FWHM value of φ_R was 0.055°. Deconvolution with (5) resulted in a mosaicity of 0.007°. (*b*) The (−9 −13 −16) reflection lies along the vertical axis. The measured FWHM value of φ_R was 0.0173° and the deconvoluted FWHM mosaicity was 0.0130°. Definitions for FWHM and FWQM are indicated. The positions of these reflections on the detector are indicated with arrows in Fig. 5.

The φ position of the maximum value of the reflection was then located and the width of the reflections was calculated as FWHM and full-width at quarter-maximum (FWQM) values (Fig. 3).

Multiple Gaussian functions were automatically fitted to all the reflection profiles with $I/\sigma(I) > 5.0$ using MATLAB subroutines. For each reflection, a range of data that was three times the FWQM value about the reflection maximum was used. Two Gaussians fit the reflection profiles optimally. Use of three Gaussians did not significantly reduce the residual. The automatic curve-fitting routine initially placed one Gaussian at the maximum and one at the FWQM value to the right or left

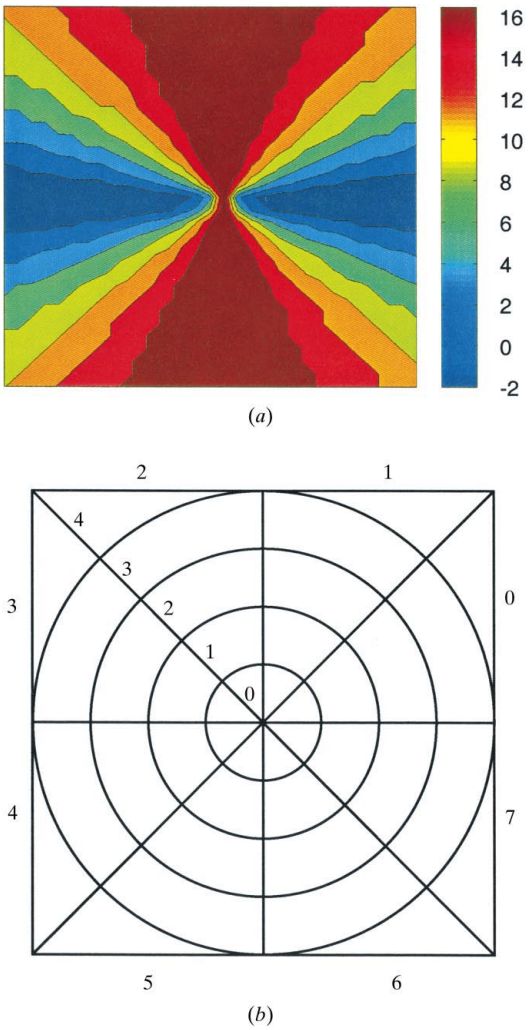

Figure 4
Analysis of corrections applied and definition of detector sectors and rings. (*a*) The corrections for beam characteristics and the Lorentz factor applied to the area-detector surface. This plot was generated by creating artificial φ_R data with a constant value of 0.020° on a two-dimensional grid across the detector face and then applying the deconvolution equation (4) to each point. Values for the resulting η value are in thousandths of a degree. In the vertical region (dark red) small corrections (0.002) were applied, giving an η value of 0.018°; the correction increased radially towards the horizontal region (dark blue). (*b*) Definition of detector sectors and resolution rings. The upper resolution limit was 11.7, 5.9, 4.0 and 3.0 Å for rings 0, 1, 2 and 3, respectively. The rotation axis is horizontal in both parts.

of the maximum. The proper side for the second Gaussian was determined by comparing the ratio of FWHM to FWQM for each side with that of a perfect Gaussian. The Levenburg–Marquett algorithm was then used to perform a non-linear least-squares fit on the data. A constant background was applied and constrained to be greater than zero. No user intervention was required for this step.

4. Results and discussion

The first step in data processing was the determination of the unit-cell parameters and the orientation matrix with *MOSFLM*. The unit-cell parameters were $a = 100.0$, $b = 108.3$, $c = 180.7$ Å. The data from the four 1.0° images were only 9.6% complete and did not contain enough reflections to provide reliable statistics for assessment of crystal quality. Clearly, by collecting more 1.0° images one could obtain reliable $R_{\rm sym}$ and $I/\sigma(I)$ *versus* resolution statistics about the crystal. These statistics would be useful, along with the mosaicity analysis, in future comparative studies. The diffraction limit of the MnSOD crystal, defined to be the resolution where $I/\sigma(I)$ dipped below 2.0 in this relatively weak unfocussed synchrotron beam, was 3.0 Å. In comparison, data collected at the more powerful SSRL beamline 7-1 operating in focused mode from the cryocooled piece of this crystal yielded 1.3 Å resolution (Borgstahl *et al.*, 2000).

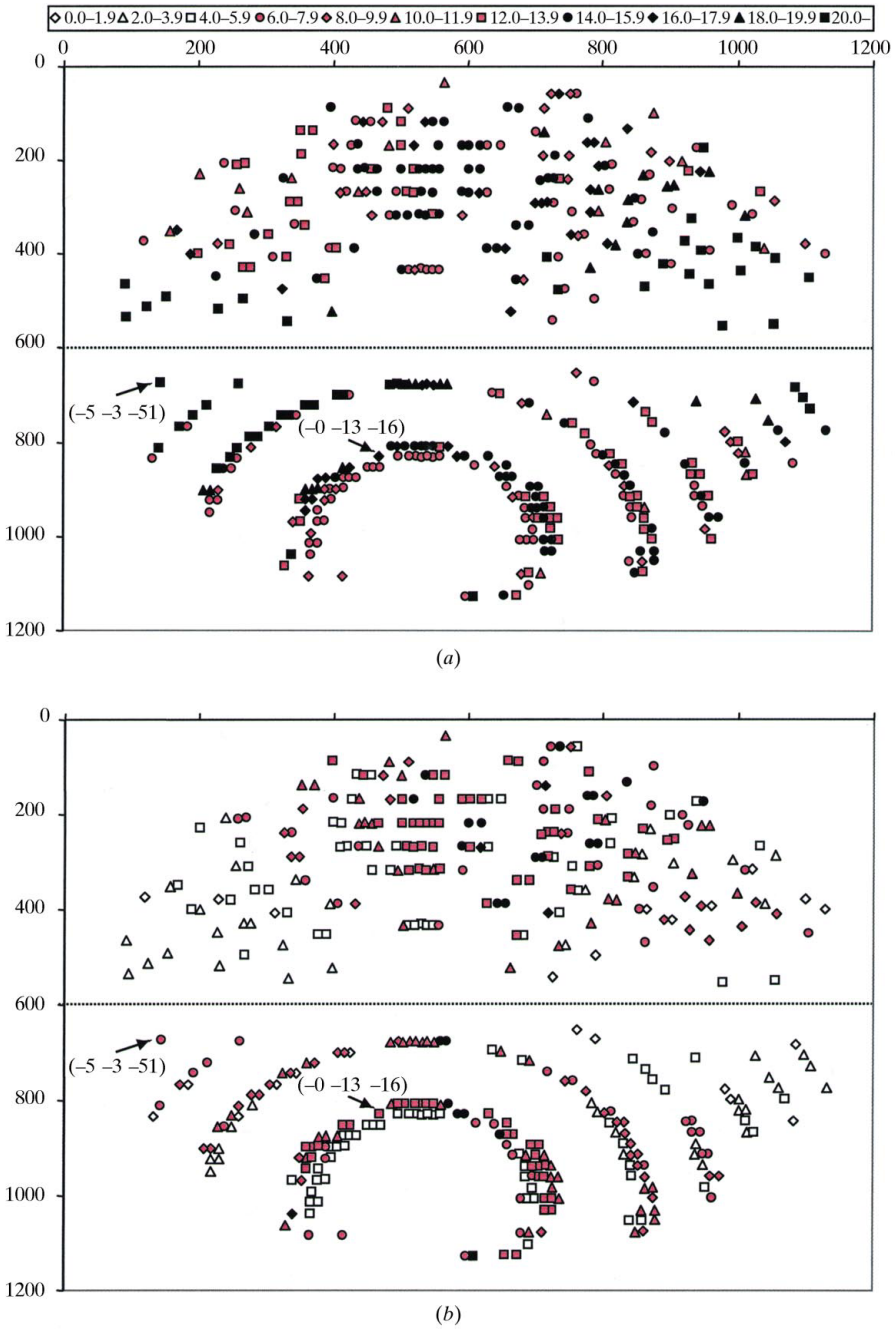

Figure 5
Measured reflection-profile widths and mosaicity plotted on the detector face (in pixels): (*a*) FWHM φ_R and (*b*) the corresponding η. For clarity, the detector dimensions are elongated along the *x* axis. A dashed line indicates the horizontal rotation axis. Pixel size was 0.1632 mm. Symbols are color coded to indicate FWHM values (in thousandths of a degree) and are grouped into three ranges. In the symbol legend above the plots, values between 0 and 5.9 are white, between 6 and 3.9 are pink and between 14 and 20 are black. Symbols within each group are ranked circle < diamond < triangle < square.

The quality of the protein crystal can be quantitatively evaluated by examining the reflection profiles (Fig. 3). Reflection profiles along the horizontal rotation axis (Fig. 3*a*) are dramatically broadened by the beam and Lorentz effects. On the other hand, the reflections recorded near the vertical equatorial axis (Fig. 3*b*) are minimally broadened and their observed widths are close to the true crystal mosaicity. For this experimental setup, the deconvolution equation (5) reduces the measured φ_R FWHM values minimally near the vertical axis and the correction increases towards the horizontal axis (Fig. 4*a*). When the FWHM values of φ_R for 1° of fine φ-slicing data are plotted according to their position on the CCD detector, the instrumental broadening along the horizontal can be seen (Fig. 5*a*). The deconvolution of φ_R to η effectively removes the instrumental broadening (Fig. 5*b*). Interestingly, the values of η across the detector face are not homogeneous (Fig. 5*b*).

From 1° of superfine φ-sliced data, the mosaicities of 260 reflections were analyzed. The FWHM mosaicity values ranged from 0.0011 to 0.0188°,

Table 1
Reciprocal space, mosaicity and relative mosaic block size statistics.

Sector average values for mosaicity, η, in thousandths of degrees are followed by the standard deviation in parentheses. The five reflections that fit with negative values for the second Gaussian were omitted from the Gaussian statistics. The percentage of the total peak area arising from the constant background is not reported.

										Peak areas (% total area)	
Ring	Sec.	$h_{min}\rightarrow h_{max}$	$k_{min}\rightarrow k_{max}$	$l_{min}\rightarrow l_{max}$	No. ref.	η FWHM	η FWQM	η Gaussian fit 1	η Gaussian fit 2	Fit 1	Fit 2
0	0				0						
1	0	3→4	7→10	14→19	2	11.4 (0.4)	15.7 (0.8)	5.2 (0.1)	8.1 (0.8)	48 (10)	42 (1)
2	0	−2→5	4→15	23→40	9	8.3 (1.8)	12.5 (2.8)	5.0 (1.5)	5.5 (1.7)	56 (7)	35 (12)
3	0	−3→5	5→17	35→48	6	8.7 (2.4)	12.5 (3.4)	4.9 (2.0)	5.8 (2.0)	56 (13)	35 (14)
Sec. 0 total		−3→5	4→17	14→48	17	8.8 (2.1)	12.9 (3.0)	5.0 (1.6)	5.9 (1.9)	55 (10)	36 (12)
0	1	2	4	6	1	11.3	17.4	5.9	7.4	57	36
1	1	4→7	8→15	2→9	6	13.5 (0.9)	18.5 (0.7)	6.5 (0.7)	8.2 (1.5)	55 (3)	38 (8)
2	1	5→10	13→22	1→26	18	13.1 (2.2)	17.5 (2.6)	6.1 (1.0)	7.5 (1.7)	54 (7)	36 (36)
3	1	7→12	21→32	1→37	18	13.3 (1.8)	18.5 (3.7)	6.5 (1.5)	7.4 (2.4)	47 (11)	31 (11)
Sec. 1 total		2→12	4→32	1→37	43	13.2 (1.9)	18.1 (2.9)	6.3 (1.2)	7.6 (1.9)	51 (9)	34 (9)
0	2				0						
1	2	6	12	−20	1	9.0	11.6	5.0	3.3	50	18
2	2	6→10	12→22	−30→−1	27	11.8 (2.0)	15.2 (2.7)	6.2 (0.9)	5.9 (1.6)	59 (7)	34 (8)
3	2	9→12	21→30	−37→−1	18	11.6 (2.6)	14.9 (2.8)	6.0 (1.0)	6.0 (1.5)	53 (9)	34 (7)
Sec. 2 total		6→13	12→33	−31→−1	47	11.6 (2.2)	15.0 (2.7)	6.1 (1.0)	5.9 (1.6)	57 (8)	33 (8)
0	3				0						
1	3	2→4	4→8	−26→−24	3	4.1 (0.9)	6.4 (1.5)	4.4 (2.1)	2.3 (0.7)	59 (0)	28 (12)
2	3	1→6	3→14	−42→−31	9	4.0 (1.3)	5.9 (1.7)	3.1 (1.0)	3.2 (1.3)	56 (5)	36 (7)
3	3	−1→8	5→22	−56→−37	11	4.1 (1.2)	6.1 (1.8)	3.2 (1.0)	3.0 (1.6)	63 (12)	30 (11)
Sec. 3 total		−1→8	3→22	−56→−24	23	4.0 (1.2)	6.1 (1.7)	3.3 (1.1)	3.0 (1.4)	60 (9)	32 (9)
0	4	−3→−3	−5→−5	−12→−11	2	10.8 (0.7)	16.0 (0.2)	5.6 (0.4)	7.5 (1.2)	55 (10)	39 (8)
1	4	−5→−3	−7→−5	−27→−13	5	9.1 (1.0)	13.7 (1.3)	5.3 (0.2)	7.0 (0.7)	57 (7)	36 (4)
2	4	−8→−4	−10→−4	−39→−28	7	9.0 (1.1)	12.9 (1.1)	5.3 (0.7)	7.4 (1.5)	56 (5)	40 (4)
3	4	−13→−5	−15→−3	−51→−39	11	8.4 (1.4)	12.2 (1.4)	5.3 (0.6)	6.3 (2.0)	58 (12)	35 (8)
Sec. 4 total		−13→−3	−15→−3	−51→−11	25	8.9 (1.3)	13.0 (1.6)	5.4 (0.5)	6.9 (1.6)	57 (9)	37 (7)
0	5	−3→−3	−5→−5	−10→−5	6	12.7 (1.8)	17.5 (1.3)	6.2 (0.4)	8.1 (1.4)	54 (11)	38 (1)
1	5	−9→−8	−13→−12	−14→−2	11	13.2 (1.5)	17.9 (1.0)	5.9 (0.5)	8.8 (1.7)	53 (10)	42 (4)
2	5	−13→−9	−17→−13	−28→−6	10	12.4 (1.0)	17.0 (0.9)	6.0 (0.7)	7.3 (1.1)	55 (8)	37 (7)
3	5	−15→−13	−19→−17	−29→−28	4	10.2 (1.8)	17.6 (2.4)	6.1 (1.2)	7.4 (1.0)	52 (7)	34 (11)
Sec. 5 total		−15→−3	−19→−5	−29→−2	31	12.5 (1.7)	17.5 (1.3)	6.0 (0.6)	8.0 (1.5)	54 (9)	39 (6)
0	6	−4	−6	4	1	11.6	16.2	5.3	8.1	52	49
1	6	−10→−5	−14→−7	2→18	7	9.8 (2.6)	13.4 (3.3)	5.2 (0.9)	5.9 (2.1)	55 (7)	34 (9)
2	6	−15→−10	−19→−12	4→26	23	11.1 (2.2)	14.3 (2.8)	5.6 (1.0)	6.0 (1.6)	58 (9)	36 (7)
3	6	−22→−15	−26→−17	6→38	18	10.6 (1.8)	14.4 (2.5)	5.6 (0.7)	6.5 (2.0)	55 (9)	37 (7)
4	6	−21→−19	−23→−19	25→37	2	9.7 (4.3)	12.2 (4.3)	4.3 (3.5)	5.9 (3.5)	51 (11)	44 (1)
Sec. 6 total		−22→−4	−26→−6	2→38	51	10.7 (2.1)	14.2 (2.8)	5.5 (0.9)	6.2 (1.8)	56 (9)	37 (7)
0	7				0						
1	7	−6→−3	−6→−3	17→26	2	3.1 (2.9)	4.7 (3.2)	1.7 (2.0)	1.8 (1.8)	47 (15)	28 (7)
2	7	−12→−7	−12→−5	28→36	5	5.1 (1.1)	6.8 (1.5)	2.9 (0.8)	2.8 (0.6)	57 (6)	36 (2)
3	7	−15→−8	−15→−2	35→53	16	4.3 (1.9)	7.0 (2.2)	3.3 (1.6)	2.9 (1.8)	58 (11)	30 (12)
Sec. 7 total		−15→−3	−15→−2	17→53	21	4.5 (1.9)	6.8 (2.2)	3.1 (1.5)	2.8 (1.6)	57 (10)	31 (10)
Total		−22→13	−26→33	−56→53	260	10.1 (3.6)	13.8 (4.5)	5.4 (1.5)	6.1 (2.3)	55 (9)	35 (9)

with an overall average of 0.0101° (s.d. 0.0036°; Table 1). What is causing this large range of values seen in the FWHM mosaicity? For asymmetric reflections with a shoulder on one side, the FWHM calculation could underestimate the width of the reflection, whereas the FWQM would be more likely to include the full width (Fig. 3). The FWQM mosaicity values ranged from 0.0024 to 0.0261°, with an average of 0.0138° (s.d. 0.0045°; Table 1). For the FWQM measurements both the average peak width and the standard deviation increased by about 1.3-fold, indicating no reduction in the scatter in the data. Therefore, underestimating the reflection width does not account for the large range of the mosaicity data (Figs. 6*a* and 6*b*). The large range is in fact an indicator of anisotropic mosaicity as is shown below.

The majority of the reflection profiles had a shoulder peak to the right of the main peak (Fig. 3*b*). Therefore, all reflection

profiles were automatically fitted with two Gaussian profiles. The primary Gaussian contributed 55% (s.d. 9%) and the secondary Gaussian contributed 35% (s.d. 9%) of the reflection. On average, the deconvoluted width of the first Gaussian was 0.0054° (s.d. 0.0015°) and the second was 0.0061° (s.d. 0.0023°). Overall, the majority of the data were fitted well with two Gaussians. Five reflections gave a negative deconvoluted width for the second Gaussian (Fig. 6*c*), indicating that they could have been better fitted with a single Gaussian. Table 1 shows that the fraction of the reflection intensity attributed to each Gaussian remains relatively constant throughout the data set. This indicates that the two-Gaussian model is well matched to this data set.

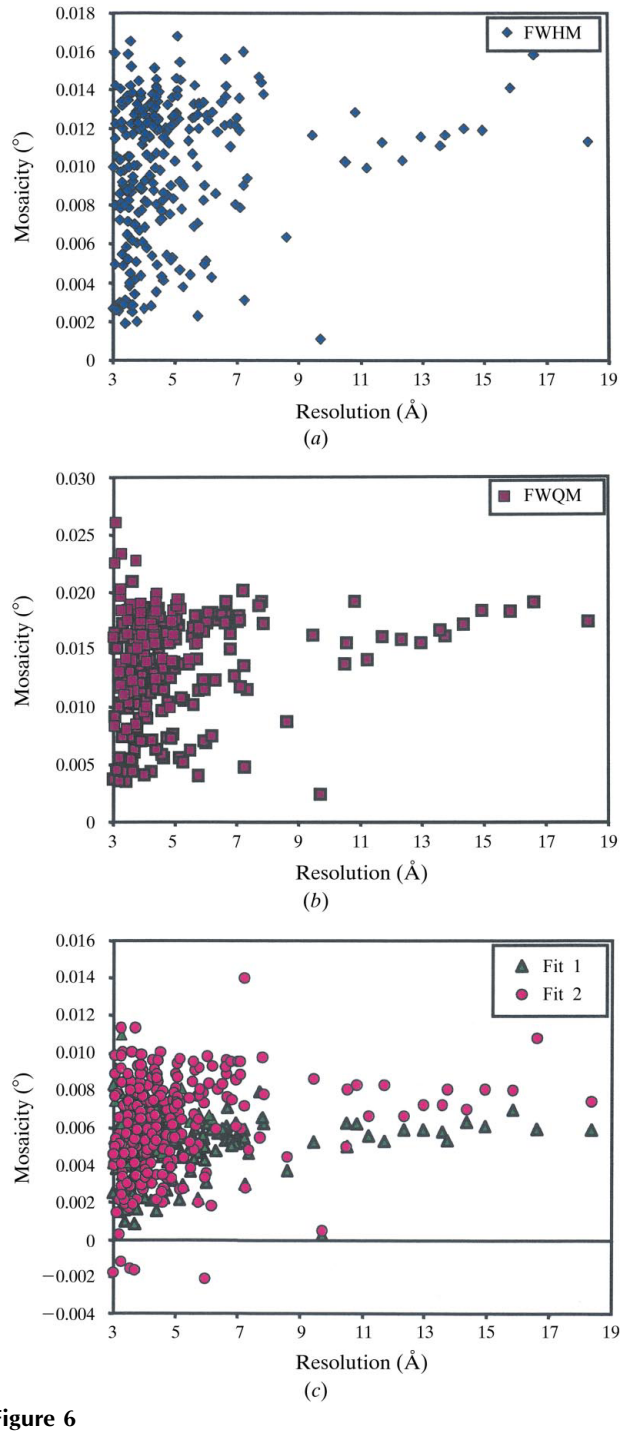

Figure 6
Plot of mosaicity against resolution for all data for (*a*) FWHM, (*b*) FWQM and (*c*) each Gaussian.

The data in Table 1 also show that the symmetry-related sectors (*e.g.* 0 and 4) have very similar mosaicity values (see also Fig. 5*b*). The internal consistency of the data is also shown by the results for the symmetry-related reflections in Table 2. Table 1 also shows that although the mosaicity varies considerably between the sectors, within each sector the mosaicity does not vary greatly with resolution. The observed dependence of mosaicity on direction but not resolution is to be expected from a crystal exhibiting anisotropic mosaicity, whereas errors in the deconvolution formula or the beam parameters would be expected to produce resolution-dependent effects.

The relative contributions of domain misalignment and volume can be distinguished from the variation of d spacing within a domain by studying mosaicity as a function of resolution. Domain-misalignment and volume effects are independent of resolution, whereas mosaicity arising from variation of d spacing is dependent on resolution. For isotropic mosaicity, this is a simple test; however, the MnSOD data shows significant anisotropy. The plot of mosaicity *versus* resolution (Fig. 6) indicates that the mosaicity is fairly constant at low resolution and variable at higher resolution. The increase in variability with resolution is probably a consequence of the anisotropic mosaicity.

The anisotropic nature of crystal mosaicity was illustrated by Snell *et al.* (1997) as a three-dimensional vector plot. The individual reflection's mosaicity was the vector magnitude and the indices were the direction. Ferrer & Roth (1998) later introduced an anisotropic mosaicity model given by

$$\eta_{hkl}^{\rm calc} = \frac{\eta_h h^2 + \eta_k k^2 + \eta_l l^2}{h^2 + k^2 + l^2}. \qquad (6)$$

Here, η_h, η_k and η_l represent the anisotropic components of mosaicity. With this model, η_h, η_k and η_l were calculated using a matrix representation of multivariate regression analysis of all 260 measured mosaicity values. For the MnSOD crystals, FWHM values of η_h, η_k and η_l were 0.0068, 0.0140 and 0.0046°, respectively. Inspection of the mosaicity values and their indices (Tables 2 and 3) shows that mosaicity is large when l is low and *vice versa*. In addition, when a group of reflections with constant values of h and k was studied it was seen that as l increases mosaicity decreases. Because this is a very narrow set of data, the range of h indices is less than that for k and l and therefore information on the crystal properties along the h direction is less certain than in the other two directions. The data indicate that the crystal is most perfectly ordered along the c direction. The c direction contains a twofold screw axis, corresponds to the longest unit-cell dimension and lies along the length of the needle-shaped crystal (Fig. 1). The direction of highest perfection therefore lies along the direction of favored growth. The reduction of mosaicity in this direction is similar to that seen for another needle-shaped crystal, apocrustacyanin C1 (Snell *et al.*, 1997).

Table 2
Examples of the strongest reflections and symmetry-related diffraction data.

FWHM and FWQM in thousandths of degrees.

									Gaussian fit 1			Gaussian fit 2		
h	*k*	*l*	*d* (Å)	I_{max}	η FWHM	η FWQM	Ring	Sec.	*I*	η FWHM	Area (%)	*I*	η FWHM	Area (%)
The strongest reflection in each sector of ring 1														
4	10	19	6.8	1053	11.1	15.1	1	0	971	5.1	55	572	7.5	43
6	12	2	7.9	1800	13.8	17.3	1	1	1814	6.2	56	1035	7.8	39
6	12	−20	6.0	146	9.0	11.6	1	2	131	5.0	50	61	3.3	18
2	4	−24	7.2	2082	3.1	4.8	1	3	1297	3.0	59	845	2.8	37
−3	−5	−14	10.5	841	10.3	15.6	1	4	696	5.0	48	441	8.1	43
−8	−12	−8	7.0	974	12.5	17.4	1	5	929	5.6	55	529	9.0	46
−7	−9	16	7.1	686	7.9	11.7	1	6	578	5.3	59	288	5.4	30
−3	−3	17	9.7	1500	1.1	2.4	1	7	1286	0.3	58	663	0.5	32
The strongest reflection in each sector of ring 3														
1	11	43	3.9	596	8.9	12.1	3	0	490	5.4	60	275	7.1	40
8	22	27	3.8	702	13.3	16.3	3	1	634	6.1	53	376	7.2	36
11	25	−10	3.8	471	14.5	18.5	3	2	406	6.9	48	281	8.1	38
7	17	−37	3.7	635	5.1	8.5	3	3	447	4.6	63	254	5.0	38
−9	−11	−39	3.9	862	8.8	12.7	3	4	757	5.2	61	416	6.4	39
−13	−17	−29	3.9	278	8.8	15.3	3	5	257	5.9	61	125	7.6	36
−17	−21	11	3.8	588	12.6	17.6	3	6	532	5.6	44	362	8.8	45
−13	−13	36	3.8	560	6.1	7.9	3	7	422	4.7	65	303	2.9	34
Symmetry-related reflections														
11	25	1	3.9	362	13.0	18.3	3	1	337	5.9	46	183	9.4	37
11	25	−1	3.9	323	13.9	17.6	3	2	330	7.0	61	201	6.5	35
10	22	1	4.4	840	14.2	18.4	2	1	777	6.4	51	506	8.7	43
10	22	−1	4.4	824	14.6	19.2	2	2	771	6.6	55	497	8.9	46
9	19	1	5.1	208	16.8	19.4	2	1	188	6.3	39	126	7.3	29
9	19	−1	5.1	225	13.7	18.8	2	2	219	5.9	49	134	8.7	42

Shaikevitch & Kam (1981) suggest that lattice errors, local or extended, cause dislocations and therefore a tilt angle between mosaic domains. These lattice errors can propagate by two methods: accumulation of systematic errors or a random statistical distribution. Systematic errors will be linearly proportional to the number of unit cells, whereas random errors are proportional to the square root of the number of cells. The MnSOD mosaicity data indicates that systematic rather than random errors exist in the MnSOD crystal. Combining Shaikevitch & Kam's systematic error model and the calculated anisotropic mosaicity values (η_h = 0.0068, η_k = 0.0140, η_l = 0.0046°) gives an average mosaic block with dimensions 83, 44 and 223 µm along *h, k* and *l*, respectively. The crystal is approximately 250 µm long in the *c* direction or about the calculated domain size (Fig. 1). In the other directions, two or more blocks could fit within the dimensions of the crystal. The alternative random-error model gives a mosaic block size that encompasses the entire crystal in all three dimensions. In the analysis of the MnSOD crystal, all of the reflections were automatically fitted with two Gaussians and for the large majority of the reflections the two Gaussians assumed a fairly constant percentage ratio of 55:35 on average. However, nine reflections were primarily composed of one Gaussian (Table 4) and for 20 reflections the smaller second Gaussian is only 10–25% of the total reflection. Table 4 shows that for all but one of the single-Gaussian reflections *l* is much larger than *h* or *k*, which is consistent with the low calculated mosaicity along the *l* direction. Although the narrow range of the data and the limited number of reflections used in this preliminary study does not permit a statistical assessment, these results support the systematic error model and not the random-error model that predicts a crystal of this size to be a single block.

5. Conclusions

This MnSOD crystal was a challenging sample to evaluate owing to its large unit cell and asymmetric reflection profiles. There was a large variation in mosaicity over the range of reflections examined. Using the fine-slicing method with synchrotron radiation and a fast-readout CCD detector, crystal mosaicity was evaluated using 260 reflections from 1° of data. The reflections were recorded simultaneously at different resolutions and indexed to facilitate sample comparison. The same experimental setup allows the collection of conventional rotation data so that the conventional crystallographic parameters R_{sym} and $I/\sigma(I)$ can be used in the comparison. The ability to record a large amount of mosaicity data rapidly from a single sample allows a more robust statistical analysis of crystal quality than had previously been achieved. This method has also been successfully applied to investigate the mosaicity of lysozyme crystals and insulin crystals both at room temperature and cryocooled for both

Table 3
Examples of anisotropy in the diffraction data.

FWHM and FWQM in thousandths of degrees.

									Gaussian fit 1			Gaussian fit 2		
h	*k*	*l*	*d* (Å)	I_{max}	η FWHM	η FWQM	Ring	Sec.	*I*	η FWHM	Area (%)	*I*	η FWHM	Area (%)
Mosaicity is large when *l* is low														
6	12	2	7.9	1800	13.8	17.3	1	1	1814	6.2	56	1035	7.8	39
−9	−13	2	6.6	434	13.7	18.0	1	6	435	5.7	55	258	8.4	46
11	25	1	3.9	362	13.0	18.3	3	1	337	5.9	46	183	9.4	37
10	22	1	4.4	840	14.2	18.4	2	1	777	6.4	51	506	8.7	43
9	19	1	5.1	208	16.8	19.4	2	1	188	6.3	39	126	7.3	29
11	25	−1	3.9	323	13.9	17.6	3	2	330	7.0	61	201	6.5	35
10	22	−1	4.4	824	14.6	19.2	2	2	771	6.6	55	497	8.9	46
9	19	−1	5.1	225	13.7	18.8	2	2	219	5.9	49	134	8.7	42
11	25	−2	3.9	309	13.6	19.1	3	2	293	8.0	67	152	6.9	30
9	19	−2	5.0	324	14.6	18.9	2	2	309	6.9	59	198	7.4	40
−9	−13	−2	6.7	410	14.2	18.2	1	5	395	7.1	63	227	7.1	36
Mosaicity is small when *l* is high and *h* and *k* are low														
1	5	−42	4.2	805	2.8	4.4	2	3	494	2.1	52	306	4.2	45
1	3	−31	5.8	408	2.3	4.0	2	3	264	2.2	60	169	2.0	37
0	6	−53	3.3	541	2.9	4.4	3	3	363	2.2	54	210	2.2	31
−1	5	−56	3.2	505	2.5	3.6	3	3	415	1.5	65	216	0.3	24
−2	4	40	4.4	185	4.9	6.3	2	0	131	1.6	43	121	3.5	57
−3	5	48	3.7	435	4.2	6.3	3	0	329	0.8	38	259	4.1	56
−3	−3	17	9.7	1500	1.1	2.4	1	7	1286	0.3	58	663	0.5	32
As *l* increases mosaicity decreases														
−3	−5	−5	16.6	1412	15.8	19.1	0	5	1077	6.0	33	755	10.8	38
−3	−5	−6	15.8	2035	14.1	18.3	0	5	1884	7.0	60	1005	8.0	36
−3	−5	−7	14.9	1540	11.9	18.4	0	5	1491	6.1	58	809	8.1	40
−3	−5	−8	14.3	880	12.0	17.2	0	5	829	6.3	62	455	7.0	37
−3	−5	−9	13.6	666	11.1	16.7	0	5	619	5.8	55	350	7.3	37
−3	−5	−10	13.0	893	11.5	15.6	0	5	811	5.9	59	465	7.3	39
−3	−5	−11	12.3	3547	10.3	15.9	0	4	3353	5.9	62	1655	6.6	33
−3	−5	−12	11.7	1194	11.3	16.1	0	4	998	5.3	49	658	8.3	45
−3	−5	−13	11.2	638	10.0	14.1	1	4	604	5.6	64	299	6.7	36
−3	−5	−14	10.5	841	10.3	15.6	1	4	696	5.0	48	441	8.1	43

Table 4
Examples of data with primarily one Gaussian.

Mosaicity values are reported as FWHM in °.

							Area (%)	
h	*k*	*l*	*d* (Å)	η total	η fit 1	η fit 2	Fit 1	Fit 2
−11	−9	42	3.7	0.0034	0.0037	−0.0022	93	0
−12	−6	55	3.0	0.0027	0.0025	−0.0023	100	1
4	8	−26	6.0	0.0050	0.0043	−0.0021	77	1
−12	−10	43	3.5	0.0029	0.0029	−0.0021	41	1
5	13	−40	3.9	0.0043	0.0044	0.0029	92	1
9	23	−37	3.2	0.0078	0.0073	−0.0012	97	1
12	30	7	3.3	0.0134	0.0105	0.0024	35	3
−15	−15	36	3.5	0.0079	0.0068	0.0011	85	7
−11	−9	41	3.8	0.0020	0.0016	0.0016	41	7

microgravity and ground-grown crystals (manuscripts in preparation).

Three types of crystal imperfections contribute to increased mosaicity: domain misalignment, domain volume and defect or impurity incorporation (Boggon *et al.*, 2000; Nave, 1999). The measured mosaicity contains information that can be used to identify the type of imperfections existing within a crystal sample. Volume and misalignment effects are independent of resolution and it is not possible to distinguish between the two with mosaicity analysis alone. Variation of *d* spacing owing to defect or impurity incorporation is dependent on resolution, but no clear resolution trends exist in the MnSOD data. The superfine φ-slicing method will be improved by collecting a greater range of data on each crystal. More 1° oscillations will be measured to obtain better statistics in the R_{sym} and $I/\sigma(I)$ calculations and at least two swaths of 0.001° data 90° apart will be collected to improve the anisotropic η calculation. More superfine φ-sliced data will allow the anisotropic η calculation to be performed in resolution bins in order to determine the contributions of domain misalignment, domain volume and variation of *d* spacing within a domain to the mosaicity.

Two additional pieces of information are contained in the data once it has been fitted with two or more Gaussian peaks. Firstly, the angular separation between multiple peaks can measure the misalignment of discrete domains. Secondly, the anisotropic η calculation could be applied to each Gaussian peak. It is not appropriate to apply either of these analyses to the MnSOD sample owing to the limited area of reciprocal space collected. The collection of at least two orthogonal swaths of the superfine φ-sliced data is necessary for this form of analysis. The approximation of the reflection profile to the sum of two Gaussians appears to be reasonable as shown by the large (∼90%) and relatively constant fraction of the intensity accounted for by the two Gaussians. A more theoretically rigorous and computationally intensive method would be a Fourier deconvolution of the true crystal mosaicity (Snell, 1998). This was not necessary for the analysis of the MnSOD crystal, but for crystals with reflection profiles composed of many components the Fourier method will probably be mandatory.

The software used in this analysis can be obtained on a collaborative basis from the authors. This work was funded by NASA grants NAG8-1380. EHS held a National Research Council (MSFC) Research Associateship and was supported by a NASA Advanced Technology Development grant and NASA grant NCC8-66(3537-1). This work is based upon

research conducted at the Stanford Synchrotron Radiation Laboratory (SSRL), which is funded by the Department of Energy, Office of Basic Energy Sciences. The Biotechnology Program is supported by the National Institutes of Health, National Center for Research Resources, Biomedical Technology Program and the Department of Energy, Office of Biological and Environmental Research. We would like to thank Andy Arvai, Chris Nielsen and Nguyen-huu Xuong for useful discussions early in this work and for access to unpublished software. We would like to acknowledge help from and discussions with Samuil Belopolskiy, Zofia Rek, Walter Pangborn, David Smith, Bob Blessing, Mark Van der Woerd, Andrew Leslie and John Helliwell during this work.

References

Boggon, T. J., Helliwell, J. R., Judge, R. A., Olczak, A., Siddons, D. P., Snell, E. H. & Stojanoff, V. (2000). *Acta Cryst.* D**56**, 868–880.
Borgstahl, G. E. O., Pokross, M., Chehab, R., Sekher, A. & Snell, E. H. (2000). *J. Mol. Biol.* **296**, 951–959.
Colapietro, M., Cappuccio, G., Marciante, C., Pifferi, A., Spagna, R. & Helliwell, J. R. (1992). *J. Appl. Cryst.* **25**, 192–194.
Collaborative Computational Project, Number 4 (1994). *Acta Cryst.* D**50**, 760–763.
Darwin, C. G. (1922). *Philos. Mag.* **43**, 800–829.
Evans, P. R. (1997). In *Proceedings of the CCP4 Study Weekend. Recent Advances in Phasing*, edited by K. S. Wilson, G. Davies, A. W. Ashton & S. Bailey. Warrington: Daresbury Laboratory.
Ferrer, J. L. & Roth, M. (1998). *J. Appl. Cryst.* **31**, 523–532.
Fourme, R., Ducruix, A., Riès-Kautt, M. & Capelle, B. (1995). *J. Synchrotron Rad.* **2**, 136–142.
Greenhough, T. J. & Helliwell, J. R. (1982). *J. Appl. Cryst.* **15**, 338–351.
Helliwell, J. R. (1988). *J. Cryst. Growth*, **90**, 259–272.
Helliwell, J. R. (1992). *Macromolecular Crystallography with Synchrotron Radiation*. Cambridge University Press.
Kabsch, W. (1988). *J. Appl. Cryst.* **21**, 916–924.
Leslie, A. G. W. (1990). *Crystallographic Computing*, edited by V. D. Moras, A. D. Podjarny & J. C. Thierry, pp. 27–38. Oxford University Press.
Leslie, A. G. W. (1999). *Acta Cryst.* D**55**, 1696–1702.
Lovelace, J., Snell, E. H., Pokross, M., Arvai A. S., Nielsen, C., Xuong, N.-H., Bellamy, H. D. & Borgstahl, G. E. O. (2000). *J. Appl. Cryst.* **33**, 1187–1188.
Margaritondo, G. (1995). *J. Synchrotron Rad.* **2**, 148–154.
Nave, C. (1998). *Acta Cryst.* D**54**, 848–843.
Nave, C. (1999). *Acta Cryst.* D**55**, 1663–1668.
Ng, J., Lorber, B., Giegé, R., Koszelak, S., Day, J., Greenwood, A. & McPherson, A. (1997). *Acta Cryst.* D**53**, 724–733.
Powell, H. R. (1999). *Acta Cryst.* D**55**, 1690–1695.
Shaikevitch, A. & Kam, Z. (1981). *Acta Cryst.* A**37**, 871–875.
Snell, E. H. (1998). *Proceedings of the Spacebound 1997 Meeting*, pp. 306–315. Canadian Space Agency.
Snell, E. H., Cassetta, A., Helliwell, J. R., Boggon, T. J., Chayen, N. E., Weckert, E., Hölzer, K., Schroer, K., Gordon, E. J. & Zagalsky, P. F. (1997). *Acta Cryst.* D**53**, 231–239.
Snell, E. H., Weisgerber, S., Helliwell, J. R., Weckert, E., Holzer, K. & Schroer, K. (1995). *Acta Cryst.* D**51**, 1099–1102.
Steller, I., Bolotovsky, R. & Rossman, M. G. (1997). *J. Appl. Cryst.* **30**, 1036–1040.